

# Microstructure evolution characteristics and mechanical properties of a novel nitrogenous nickel-based deposited metal from gas metal arc welding to heat treatment

Yingdi Wang<sup>1,2</sup>, Guiqing Zhang<sup>1</sup>, Taisen Yang<sup>1</sup>, Xuwei Liang<sup>1</sup>, Yunhai Su<sup>1,\*</sup>

<sup>1</sup> School of Materials Science and Engineering, Shenyang University of Technology, Shenyang 110870, China

<sup>2</sup> Department of Transportation Engineering, Yantai Vocational College, Yantai, 264670, China

**Abstract:** Nitrogenous nickel-based deposited metal was prepared by gas metal arc welding. Subsequently, solid solution treatment as well as solution and aging treatments were carried out to study the evolution of microstructure and tensile properties in different states. The results show that the high temperature tensile strength of the deposited metal exhibits good performance with the addition of W and N. The grain size of the alloy is large and petal-like Laves phase appears at the grain boundaries. After solid solution treatment, the grain size decreased and the Laves phase disappeared. However, the yield strength and elongation of the deposited metal decreased. The grain size of the solid solution and aging treated samples was more uniform. Nanoscale M(C,N) phases precipitated within the crystals and  $M_{23}C_6$  phase formed at grain boundaries. The yield strength and ultimate tensile strength were higher than the other samples, but the plasticity was the lowest. The main deformation mechanism is the unit dislocation  $a/2\langle 110 \rangle$  cutting precipitation phase.

**Key words:** nitrogenous deposited metals; microstructure; tensile performance; Dislocation;

Ultra-supercritical power generation units, as an efficient and environmentally friendly future power generation choice, are increasingly receiving attention and attention from people. The commonly used materials for ultra supercritical power generation units are iron-based alloys and nickel-based alloys. In contrast, nickel-based alloys have high temperature resistance and corrosion resistance, and can operate safely in high-temperature and high-pressure environments. At present, the most operating unit in the world is the 600 °C ultra-supercritical power generation unit. There are many types of nickel-based high-temperature alloys, which are considered the preferred materials for welding advanced ultra-supercritical (AUSC) boilers due to their excellent corrosion resistance, oxidation resistance, good tensile and fatigue properties<sup>[1]</sup>. The AUSC boiler is composed of components that are made of various materials, and this creates a necessity to weld advanced austenitic steels to nickel-based superalloys. Inconel 625 alloy exhibits excellent mechanical properties from low temperature to 980 °C. Inconel 625 filler wire can adapt to the chemical composition and thermal expansion differences between different metals,

making it suitable for welding different metals<sup>[2,3]</sup>. It can significantly improve the high-temperature mechanical properties of welded joints<sup>[4,5]</sup>. However, the continuous rise in nickel ore prices has led to a constant increase in the cost of nickel-based welding materials. Therefore, it is necessary to develop a new type of low-nickel welding consumables with excellent performance. Nickel-based alloys are typical solid solution strengthened high-temperature alloys. Thus, transition group elements such as Mo, Co, Nb, and Hf, have been added to the newly developed nickel-based welding consumables to enhance solid solution strength. At the same time, a certain amount of transition element W has also been added to the developed nitrogenous nickel-based welding materials. Transition group elements help alloys achieve excellent mechanical properties at high temperatures. It can not only reduce the diffusion ability of other alloying elements, but also lower the stacking fault energy of the alloy<sup>[6-10]</sup>. The presence of refractory alloy element tungsten and boundary strengthening element C can provide high thermal fatigue resistance for the alloy and have beneficial effects<sup>[11]</sup>. At the same time, the Ti element was added, and studies have shown that

nanostructured W-Ti exhibits significant high-temperature stability<sup>[12]</sup>. Nitrogen has a strong stabilizing effect on austenite. Therefore, adding nitrogen to alloys can improve the strength of austenitic stainless steel<sup>[13]</sup>. The presence of nitrogen can lead to the formation of carbonitrides in alloys, which are more stable than carbides<sup>[14]</sup>. Therefore, these elements have a very positive effect on the high-temperature creep resistance of nickel-based alloys.

The precipitates in the nickel-based high-temperature alloys usually include  $\gamma'$  Phase, carbide phase,  $\delta$  phase, and Laves phase. These residues also have a significant impact on the properties of the alloy. T. Liu et al. studied the fracture properties of long-term thermal exposure on microstructure and stress rupture properties of GH3535 superalloy. They found that cracks originated at the interface between M<sub>6</sub>C carbides and the matrix, resulting in a lower creep fracture life<sup>[15]</sup>. L. Z. He found that grain boundaries promote the precipitation of M<sub>23</sub>C<sub>6</sub>, and the small M<sub>23</sub>C<sub>6</sub> located at the grain boundary strengthens the boundary and effectively prevents grain boundary migration<sup>[16]</sup>. It was found that the formation of  $\gamma'$  phase promotes the transformation of MC phase to M<sub>23</sub>C<sub>6</sub> phase<sup>[17]</sup>. Microcracks can form near or inside the MC degradation zone and are detrimental to the high-temperature strength of the alloy, especially when MC is present at the grain boundary<sup>[18]</sup>. The Laves phase in nickel-based superalloys is called the undesired phase. The segregation of Laves phase will consume a large amount of solid solution strengthening elements in the alloy, thereby reducing the high-temperature strength of the alloy. Post-treatment in the form of homogenizing heat treatment is an effective method of eliminating the harmful Laves phases<sup>[19]</sup>. In addition, the distribution and size of the  $\gamma'$  phase have a considerable impact on the tensile strength of nickel-based alloys at elevated temperatures<sup>[20]</sup>. In addition, solid solution treatment also has a significant impact on the properties of nickel-based alloys. Safarzade et al.<sup>[21]</sup> studied the properties of Inconel 625 alloy fabricated by gas metal arc welding method and found that solution heat treatment reduced the elongation of the alloy, but increased its hardness and yield strength. Mathieu Ternier<sup>[22]</sup> studied the characteristics of nickel-based alloys produced by the laser-powder bed fusion (LPBF) method in different states and found that the microstructure of the alloys changed obviously with various heat treatment methods. Huan Wang et al.<sup>[23]</sup> found that by controlling the heat treatment

temperature, the grain size, grain boundary characteristics, and dislocation density of the alloy can be adjusted, thereby affecting the mechanical properties of the alloy. Mostafaei<sup>[24]</sup> believes that aging treatment improves the microhardness and tensile strength of the sample, but reduces plasticity.

This study based on the composition of Inconel 625 welding material, a certain proportion of N and W elements were added, and the content of Fe and Mn elements was increased to obtain a nickel-based alloy with lower cost and good mechanical properties. This new type of welding material is called nitrogenous nickel-based flux-cored welding wire. In this paper, the microstructure and mechanical properties of nitrogenous nickel-based flux-cored wire-deposited metal under different conditions were investigated. This study is expected to provide reliable data to support the design of low-cost alloys for ultra-supercritical material applications.

## 1. Experimental

This article is based on Inconel 625 welding material and uses JMatpro software for composition design. The nitrogenous nickel-based flux-cored wire used in this experiment is 1.2 mm in diameter, and the optimal chemical composition (mass fraction, %) is: 0.1C, 2.5Mn, 0.45Si, 0.2Cu, 41Ni, 1.3Ti, 1.5Al, 22Cr, 4.5Mo, 5.00Nb, 4.0W, 0.55N, P<0.001, S<0.001, and rest Fe. The material was deposited on a 304L stainless steel plate with a YD-500FR2 gas-shielded welding machine, layer by layer. Each pass was deposited in opposite direction to the previous one with 3 min interval between subsequent passes during welding to control the temperature between passes not exceeding 150 °C. In addition, the protective gas is 97% argon and 3% nitrogen, which inhibit weld metal oxidation during welding. The deposition parameters of the overlays include a welding current of 180 A, a welding speed of 25cm /min, and welding voltage is 25V. Thereafter, 180 mm in length and 12 mm in height walls with 4 overlay welding passes were fabricated. Three similar walls were fabricated and the macrograph of the wall is shown in Fig. 1. One of them was characterized in the as-deposited state, while the others were subjected to post-processing heat treatment and subsequent characterization.

In order to find the exact solution treatment temperature, DSC test was carried out on the prepared sample. A cylindrical DSC sample of 3 mm × 2 mm was cut off from the deposited metal by a

wire-cutting machine, and the oxide scale on the surface was removed by sandpaper and cleaned by ultrasonic for 5 min. The instrument used in this experiment is the THEMYS comprehensive analyzer, with a protective atmosphere of argon gas with a flow rate of 20ml/min. The processed sample is placed in an alumina dry pot, with a testing temperature range of 800 °C -1400 °C and a heating rate of 10 °C/min.

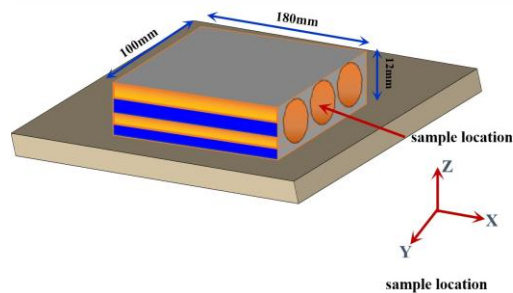


Fig.1 Schematics of deposition path (unit: mm)

To obtain a homogeneous microstructure, the remaining two cladding samples were solution heat treated (ST) in an electric furnace at  $(1080 \pm 5) ^\circ\text{C}$  for 4 h and then quenched in water. Subsequently one of them was aged (SA) at  $700^\circ\text{C}$  for 24 h and then air cooled. The heating rate of the solid solution treatment was  $10^\circ\text{C}/\text{min}$  up to  $600^\circ\text{C}$  and  $2^\circ\text{C}/\text{min}$  above  $600^\circ\text{C}$ . To investigate the effect of heat treatment on the mechanical properties of the alloys, high temperature tensile tests were carried out on the alloy specimens both in the as-deposited state and after heat treatment state. Tensile tests were performed on an MST Landmark 370.10 microcomputer-controlled electro-hydraulic servo tester with the temperature set at  $600^\circ\text{C}$ . The specimens were heated to the set temperature at a ramp rate of  $1^\circ\text{C}/\text{s}$  and held for 10 min and then the test was started at a constant tensile rate of 0.1 mm/min until the end of samples fracture. The schematic diagram of the stretching device is shown in Figure 2.

The phase composition of the deposited metal was characterized by an X-ray diffractometer, model XRD-7000, and the scanning range is  $20^\circ$ - $100^\circ$ . The as-deposited sample was chemically etched with aqua regia (HCl:  $\text{HNO}_3=3:1$ ) for 20s at room temperature to observe the microstructural features. Tensile fracture morphology was observed using BX60M optical microscope (OM) and scanning electron microscope (SEM), while microstructure and elemental analysis were performed using a field emission scanning electron

microscopy (FESEM, GeminiSEM-300) and energy dispersive spectroscopy (EDS). The microstructure and dislocation morphology of different samples were observed using a JEM-2100 transmission electron microscope (TEM). The crystal orientation was analyzed using electron backscatter diffraction (EBSD) and the average grain size was calculated by Oxford-HKL Channel 5 software.

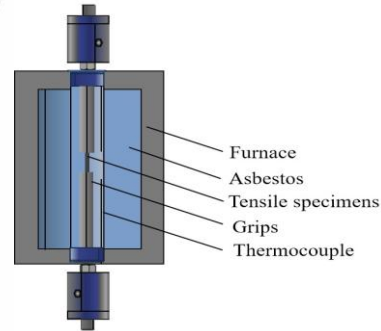


Fig. 2 Schematic diagram of tensile testing device

## 2. Results

### 2.1 Phase constituents

The phase transition temperatures of the as-deposited state deposited metals were determined by differential scanning calorimetry (DSC). The DSC curve is shown in Fig. 3(a). From the heating curve, we can see four distinct thermal reaction zones. The DSC curve is shown in Fig. 3(a). From the heating curve, there are four distinct thermal reaction zones. The first reaction region has a lower temperature and a smaller area. According to the intensity and location of the thermal reaction region, this thermal reaction region corresponds to the reaction of solid dissolution of the carbide phase in the  $\gamma$  matrix ( $896^\circ\text{C}$ ). The second region of thermal reaction is more intense. It is the temperature at which the solid phase in the alloy begins to transform to the liquid phase, i.e. the initial melting temperature of the alloy ( $1121^\circ\text{C}$ ). The solidus temperature obtained using the initial temperature extrapolation method is approximately  $1223^\circ\text{C}$ , indicating that the matrix is beginning to melt significantly. The third pronounced thermal reaction region is the endothermic reaction during the solid solution of carbonitrides ( $1242^\circ\text{C}$ ). The intensity of the endothermic peak corresponding to the fourth endothermic reaction is the most pronounced, and it is the most dominant endothermic reaction during the entire heating process, which corresponds to the melting temperature of the  $\gamma$ -phase ( $1264^\circ\text{C}$ ).

Figure 3b shows the DSC cooling curve. Four distinct exothermic peaks can be seen on the cooling

curve. The first exothermic peaks is the most important exothermic reaction during solidification and represents the precipitation temperature of the primary  $\gamma$  phase. The second exothermic peak corresponds to the precipitation reaction of carbon and nitride in the deposited metal alloy. The third exothermic peak on the curve represents the precipitation of the Laves phase. The magnitude of its peak area indirectly reflects the Laves content. The fourth exothermic peak represents the precipitation of the carbide phase.

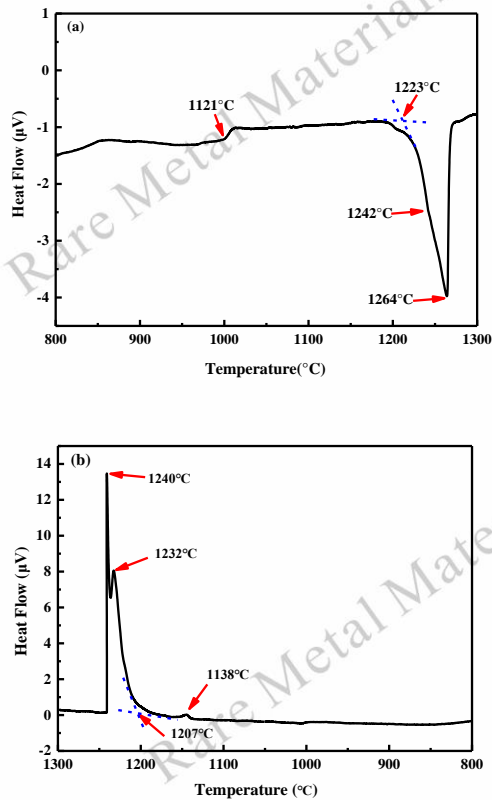


Fig. 3 DSC results of deposited metal. (a) heating curve, (b) cooling curve.

The high temperature metallographic method was used to further confirm the initial melting temperature of the alloy. It was found that a tiny melt pool appeared in the alloy at 1120°C (Fig.4b), indicating that the initial melting of the low melting point eutectic organization in the alloy started to take place, but the high temperature metallography at 1115°C did not reveal the appearance of the melt pool (Fig.4a). Therefore, by referring to the DSC curve and the metallographic organization, it can be determined that the initial melting temperature of the prepared metal is around 1115°C. In order to improve the efficiency of the solution treatment as much as possible, and make the alloy not to have

initial melting, and considering the temperature fluctuation of the furnace during the solution treatment and other factors, the solution treatment temperature of the alloy was finally set at 1110°C.

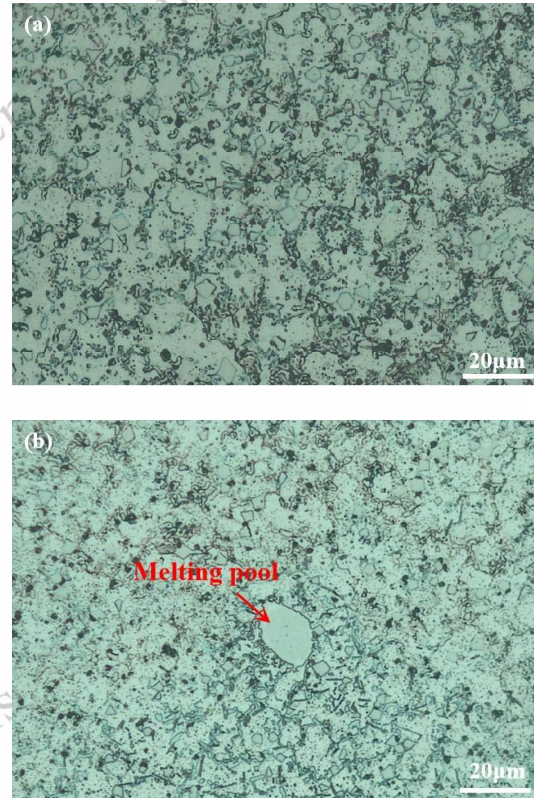


Fig. 4 Metallographic diagram of the as-deposited metal at (a) 1115°C, (b) 1120°C

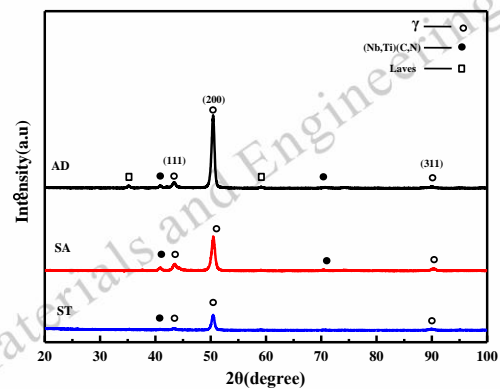


Fig.5 XRD diffraction patterns of AD, ST and SA sample

The X-ray diffraction (XRD) patterns of the samples in three different states are shown in Fig. 5. It can be seen that all the samples consist of  $\gamma$ -solid solution with FCC structure (PDF#33-0397 standard card), corresponding to (111), (200) and (311) diffraction peaks. The diffraction intensity of the (200) facet is much higher than that of the other

facets, indicating that the grains grow along the  $\langle 200 \rangle$  preferential orientation. In addition, carbon-nitride phase appeared in all three samples. The Laves phase was present in the as-deposited samples, while in the heat-treated samples, the Laves phase had disappeared. The XRD patterns can make a preliminary judgement on the phase structure of the alloys, but it is more difficult to accurately determine the constituent elements and proportions of the structures for crystal structures with similar lattice constants (e.g.,  $\gamma$  and  $\gamma'$ ).

## 2.2 Tensile behaviors

Figure 6 shows the engineering stress-strain curves, and the corresponding tensile property results are shown in Table 1. The tensile stresses remain constant until the specimens fracture, and as can be seen from the figure, all three specimens exhibit significant work-hardening behavior after yielding until the alloys fracture. The results showed that the yield strength of the as-deposited sample was 535 MPa, the ultimate tensile stress was 689 MPa and the elongation was 26.81%. after solid solution treatment. In addition, the YS and UTS of the SA-treated samples were higher than the other samples, while the elongation was the lowest. It can be seen that the work-hardening behavior of the ST sample is weakened, and the tensile strength of the ST sample is lower than that of the AD sample, while the plasticity is also weakened. The SA sample had the highest tensile strength but also the lowest plasticity among the three groups of specimens.

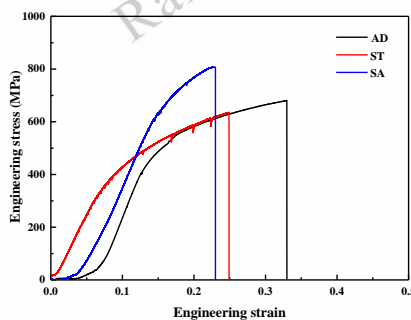


Fig. 6 Tensile engineering stress-strain curves at 600 °C.

The mechanical properties of the samples in different states are listed in Table 1. According to Table 1, it can be seen that the elongation (EL) and shrinkage (R/A) of the heat-treated samples decreased compared to the as-deposited state at 600°C, and the solid solution treatment adversely affected the strength and plasticity of the alloys, whereas the tensile strength of the SA sample was

higher than that of the AD sample by about 120 MPa, while the elongation decreased by 11%.

Tab. 1 Mechanical properties of three types of specimens at 600 °C

Sample	Yield strength (σs/MPa)	Tensile strength (σt/MPa)	Elongation (EL)	Shrinkage of section (R/A)
AD	456.51	689.01	26.81%	17.6%
ST	407.04	653.74	24.97%	16.3%
SA	535.45	811.54	23.83%	15.9%

## 2.3 Fracture morphology

The fracture characteristics of the tensile samples after fracture in different states are shown in Fig. 7, and the tensile fracture characteristics of all the samples show ductile fracture. The surface layer of the samples are relatively smooth, with shear deformation cleavage surfaces and shallow ductile dimples. Macroscopically, the fracture surface of the AD sample showed a slight necking as shown in Fig. 7a. The fracture morphology of the ST and SA samples was similar to that of the AD sample, as shown in Figures. 7(b, c), and the fracture surface was flatter in general, but there was no obvious necking phenomenon. There are a large number of ductile dimples at the fracture surface (Fig. 7d, k), accompanied by a small number of tear ribs, and the ductile dimples are the typical morphology of ductile fracture. There are fragmented carbide precipitation phases in the tough fossa of the fracture (Fig. 7j, l). There are some slip planes distributed (Fig. 7e, f), which are usually considered to be generated by dislocations slipping along the  $\{111\}$  plane, which suggests that the fracture of the samples may be caused by the stress concentration at the grain boundaries generated by dislocations slipping along the  $\{111\}$  surface<sup>[25]</sup>.

Compared with other samples, some secondary cracks existed in the surface layer of the SA sample (Fig. 7i). The formation of secondary cracks may be due to the concentration of stresses near the reinforcing and carbide phases during plastic deformation, which hinders the movement of dislocations. And when the stress concentration exceeds the tensile strength of the alloy, microcracks are produced in the stress concentration region. We know that not all microcracks eventually evolve into main cracks, but brittle fracture and cracked regions in SA sample may be caused by  $\gamma'$  phase and intergranular carbide phases<sup>[26]</sup>.

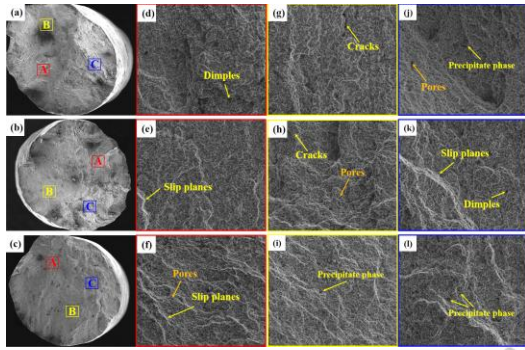


Fig. 7 SEM-SE images showing rupture surface for tensile tests at 600°C. (a)(d) (g) (j)AD and (b) (e) (h) (k)ST, (c) (f) (i) (l)SA, respectively.

In addition, to further explore the crack extension path, the longitudinal section of the tensile fracture was observed using OM, as shown in Fig.8. All the different specimens showed mixed mode fracture after stretching at 600°C. The proportion of intergranular cracks in the AD sample is larger, and most of the cracks are extended in a mixed pattern mainly along the crystal, while the proportion of perforated cracks in the specimen after heat treatment is larger, and most of the cracks are extended in the form of perforated crystals, and some fine cracks can be seen on the longitudinal section of the ST sample. There are also some micropores within the crystal of the SA sample, and with the increase of tensile force, these micropores will grow up and gather, gradually forming microcracks.

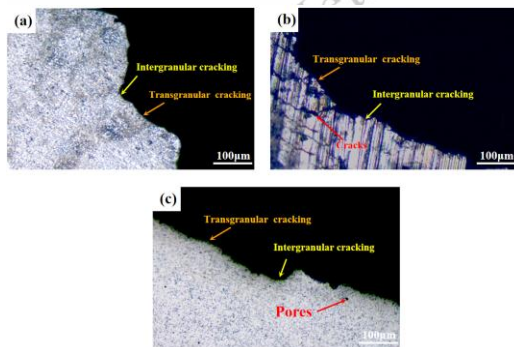


Fig.8 OM maps of typical longitudinal cross-section of fracture surface at 600 °C tensile test (a) AD and (b) ST, (c) SA, respectively.

#### 2.4 Evolution of microstructure

A large accumulation of dislocations in the matrix channels can be seen in the microstructure of the AD sample after tensile fracture at 600°C, proving that tensile stretching leads to localized deformation of the alloy, and that the dislocations are unevenly distributed in the microstructure after tensile deformation occurs (Fig.9a). Accumulation and entanglement of dislocations can be seen at grain

boundaries, leading to a rapid increase in dislocation density. The solid solution treatment results in migration of dislocations in the tissue due to thermally driven forces, release of distortion energy, etc. Dislocations are seen entangled near grain boundaries in the ST specimens. The dislocation entanglement near grain boundaries forms and eventually transitions to a cellular structure (Fig.9b). The microstructure of the aged specimen shows not only dislocations entangled near grain boundaries, but also laminar dislocations (continuous laminar dislocations) that cut through the matrix channels continuously (Fig.9c), and the dislocations are not uniformly distributed in the microstructure. The presence of laminar dislocations can reduce the density of dislocations accumulated at grain boundaries, which improves the inhomogeneity of dislocation distribution and reduces the possibility of localized deformation in the sample. Therefore, the SA sample are expected to obtain higher tensile strength, which is consistent with the results of tensile tests.

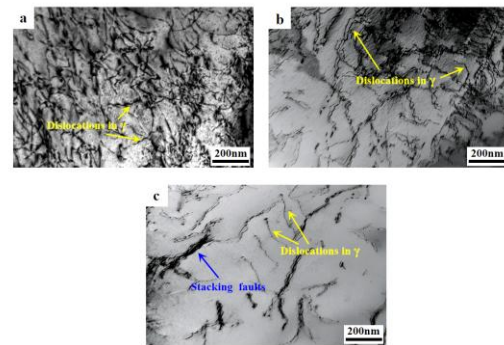


Fig.9 TEM images showing deformation microstructures at 600°C. (a) AD and (b) ST, (c)SA

#### 2.5 precipitation behavior

Fig.10 shows the distribution of liquid phase elements during the non-equilibrium solidification process of AD sample. It can be seen that, the sample is dominated by grey  $\gamma$ -Ni matrix, with bright precipitated phases distributed between the dendrites. The order of phase transformation of nitrogenous nickel-based deposited metal prepared by the GMAW method in the solidification process is as follows:  $L \rightarrow L + \gamma \rightarrow L + \gamma + MC \rightarrow L + \gamma + MC + Laves$  [27]. In the early stage of solidification the  $\gamma$ -Ni phase with fewer solute elements crystallizes first and the  $L \rightarrow L + \gamma$  crystallization process occurs; during solidification of the liquid metal, the solubility of each element in the solid-liquid phase is different. The results show that as the solidification reaction proceeds, the alloying elements, such as Mo, Nb, C,

etc., are aggregated in the inter-dendritic region, leading to the segregation behavior of the alloying elements. The occurrence of  $L \rightarrow L + \gamma + M$  (C, N), which promotes the formation of carbonitrides, was promoted. The Laves phase is a eutectic phase, which is formed in the final stage of solidification. In the prepared samples, the precipitated phases at the grain boundaries are irregularly aggregated, and the elemental distribution indicates that the precipitated phases are enriched with Mo, Nb, Cr and W elements. Thus, the deviation of Mo, Nb and C,N elements in the interdendritic zone led to the formation of some secondary phases. The EDS results of the samples after stretching at 600 °C are shown in Table 2. The bright phase elements labelled as “point 1” correspond to the  $A_2B$  structure of the Laves phase. The bulk phase marked as “point 2” was analyzed by EDS, and it can be seen that the intracrystalline precipitated phase is a composite carbon-nitride  $M(C,N)$  dominated by Mo and Nb. The results also indicate that the “point 3” position is the matrix  $\gamma$  phase, mainly containing Ni, Cr, and Fe elements with less content of other elements.

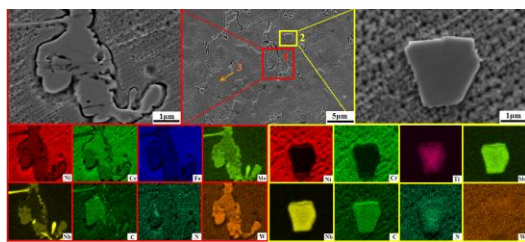


Fig. 10 Distribution of various elements in the AD sample

The distribution characteristics of elements in alloys depend on their distribution coefficient( $k$ ) in the alloy. It has shown<sup>[28,29]</sup> that during solidification, when the value of  $k$  of an element is greater than 1, the concentration of the element in the solid phase is higher than in the liquid phase, indicating that the concentration of the element in the dendritic crystals is higher than the concentration in the final solidification region. Conversely, when the  $k$  value is less than 1, the concentration of the element in the dendrite is lower than the concentration in the final solidification region. In this paper, the  $k$  values of the elements Ni, Cr, and Fe in the nitrogenous nickel-based deposited metal are all greater than 1, ( $k_{Ni}=1.07$ ;  $k_{Cr}=1.05$ ,  $k_{Fe}=1.23$ ), and the tendency to segregation of Ni and Cr is not obvious, whereas the coefficient of segregation of Fe is the largest, which indicates that the element Fe is more likely to be distributed in the solid phase. The  $k$  values of Mo and Nb, W and N elements are less than 1 ( $k_{Mo}=0.68$ ;  $k_{Nb}=0.50$ ;  $k_{W}=0.75$ ;  $k_{N}=0.94$ ), which proves that

these elements will show segregation behaviors, with the strongest segregation of Mo and Nb elements, and therefore it can be known that the inter-dendritic region, which is the final solidified region, will be enriched with a large amount of Nb and Mo elements<sup>[30]</sup>.

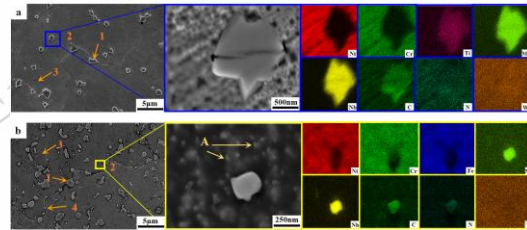


Fig. 11 Distribution of various elements of ST sample (a), SA sample (b)

As can be seen from the elemental mapping of the solid solution samples shown in Fig. 11(a), most of the precipitates have been dissolved into the matrix, with a small amount of precipitate remaining at the grain boundaries and within the boundaries. The results of the elemental analyses have confirmed that the precipitates are mainly contains N, C, Nb, and Ti elements, and the results are  $M(C, N)$  type carbides. The size of the intracrystalline precipitates is smaller than that of the AD sample, but sharp edges are still present. In Fig. 11(b). The precipitates are more homogeneous after aging, and many small particles are precipitated in the grains, which are proved to be very small  $M(C,N)$  particles (point 2) analyzed in Table 2. **The results also indicate that in the heat-treated sample, the “point 3” position is also the matrix  $\gamma$  phase, mainly containing Ni, Cr, and Fe elements with less content of other elements.** It is worth noting that the shape of the precipitates in the SA sample is more rounded, which reduces the presence of stresses in the grains. At the same time, a nanoscale phase A precipitated in the SA sample, which, it is worth pointing out, was not detected in the XRD analyses, probably due to its low content or the proximity of the lattice to the substrate, which prevented it from being detected. The precipitation position of “point 4” is mainly distributed intermittently along the grain boundary discontinuities, mainly containing C, Cr, and Mo elements. The massive carbides on the grain boundaries have been significantly reduced and some granular precipitates appear. Since the sum of the molar fractions of C, Cr and W of this precipitate is close to 1:4, it is presumed to be a  $M_{23}C_6$ -type carbide. In order to verify the accuracy of the prediction, TEM was used for detection, as shown in Fig. 12a. In addition, in Figure 11b, the position of “point 2” is

enlarged, and some ellipsoidal precipitates with a size less than  $1\mu\text{m}$  can be seen distributed within the crystal. Due to the small size of these precipitates, in order to accurately characterize them, TEM needs to be used for further detection, as shown in Figure 12b.

Tab. 2 Energy spectrum analysis of precipitates at  $600^\circ\text{C}$  (atomic fraction,%)

Sample	Position	Ni	Cr	Fe	Nb	Mo	W	Ti	C	N
AD	1	21.1	23.3	14.3	13.3	12.5	4.9	7.4	2.4	0.8
	2	2.8	2.6	1.7	23.9	4.2	4.3	5.7	41.2	13.6
	3	40.2	25.6	23.4	1.2	1.8	2.4	0.9	0.4	2.1
ST	1	2.7	2.5	1.6	23.2	3.6	6.3	4.3	41.6	15.2
	2	2.6	2.3	1.6	25.1	3.8	5.9	3.6	42.6	12.5
	3	40.2	25.6	23.4	1.2	1.8	2.4	0.9	0.4	2.1
SA	1	2.8	2.4	1.9	24.3	3.8	4.1	5.9	41.5	13.3
	2	2.8	2.6	1.7	23.9	4.2	4.3	5.7	41.2	13.6
	3	40.5	25.3	23.1	1.5	1.8	2.2	0.8	0.6	2.2
	4	3.6	60.5	1.6	2.3	8.5	1.8	6.4	15.1	0.2

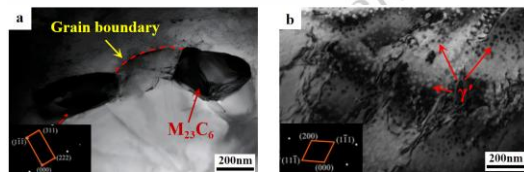


Fig. 12 TEM bright field images and electron selective diffraction pattern photos of SA sample (a) grain boundary, (b) intragranular

As shown in Fig. 12, after calibration and analysis of the diffraction spots, it was found that the precipitates at the grain boundaries were  $\text{M}_{23}\text{C}_6$ -type carbides, while the nanoscale ellipsoid-type precipitates within the crystals were  $\gamma'$  phases. Since  $\gamma$  and  $\gamma'$  are crystal structures with similar lattice constants, it is more difficult to accurately determine the constituent elements and ratios of their structures, which explains why the  $\gamma'$  phase was not detected accurately in XRD. It can also be found that the precipitates are more uniformly distributed after aging treatment, and it has been suggested that the carbide particles at grain boundaries can retard the mobile dislocations [31], and the abundance of grain boundary diffusion is more favorable to the MC decomposition process than that of intracrystalline diffusion, so that the  $\text{M}_{23}\text{C}_6$  is mainly distributed at grain boundaries or near the grain boundaries [16]. Fine-grained  $\text{M}_{23}\text{C}_6$  can effectively prevent grain boundary migration and strengthen the grain boundaries, while the precipitation of  $\gamma'$  phase can effectively improve the yield strength of the material [16,32], which is beneficial to the improvement of the strength of nickel-based alloys. It can also be seen that the element W is enriched in the precipitation phase and matrix, respectively, and the element W is also a solid solution strengthening element, so W element can make the alloy have a stronger solid solution strengthening effect, which is one of the reasons leading to the high yield strength of nitrogenous nickel-based alloys.

## 2.6 Electron backscatter diffraction analysis

The texture type of nickel-based high temperature alloys is related to process parameters such as heat input and scanning path. The IPF and PF plots of the three specimens in the XZ direction are given in Figure 13. It can be seen that the crystals of all the specimens have a stronger orientation density in the  $\{100\}$  plane, which was consistent with the XRD analysis results, i.e., the optimum orientation of the crystal structures were all  $\{100\}\langle 100\rangle$ . This is due to the fact that the initial solidification stage of the alloy during the preparation process tends to favor the preferential growth of  $\langle 100\rangle$  oriented grains towards the epitaxial columns, which ultimately leads to the formation of a strong  $\langle 100\rangle$  texture in the as-deposited sample [33].

The severe segregation that occurs during the solidification process leads to the formation of carbides and Laves phases in the interdendritic zone. In addition, directional solidification in the molten pool also leads to anisotropy of mechanical properties. Whereas, the grain size of the specimen becomes smaller after heat treatment and a large number of equiaxed grains appear, indicating the presence of recrystallisation process. And the orientation density of the ST and SA sample is stronger in the  $\{100\}$  plane. This is due to the fact that solid solution treatment produces recrystallized tissue, eliminating fine dendritic and columnar grain tissue in the prepared samples and forming equiaxed grains, which is believed to lead to more isotropic mechanical properties. Whereas the grains in the SA specimens were more uniform.

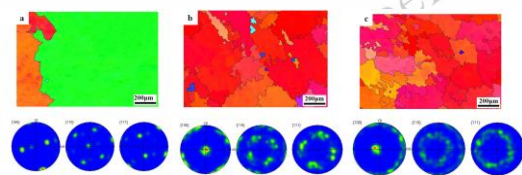


Fig.13 IPF mapping and PF mapping of (a) AD (b)ST (c) SA

Figure 14(a-c) shows the local orientation deviation of the three specimens, which reflects the degree of accumulation of deformation storage energy, and the larger value of local orientation deviation K indicates the higher degree of deformation storage energy [30]. The average values of orientation deviation K for the three specimens are  $K_{AD}=0.94$ ,  $K_{ST} = 0.81$ ,  $K_{SA}=1.32$ , respectively. It can be inferred that the SA sample has the highest degree of deformation energy storage, which is consistent with the results in Figure 6.

Figure 14(d-f) shows the distribution of Schmidt factor for the three specimens, which reflects the degree of deformation difficulty. The larger the Schmidt factor is in a particular slip system, the easier it is to initiate the slip system when the external stress is certain. It can be seen that the Schmidt factors of AD and ST sample are distributed in the range of 0.4 ~ 0.5, whereas the Schmidt factors of SA sample are distributed in the range of 0.37-0.5, and the average Schmidt coefficients of the three specimens are calculated to be 0.45, 0.48, and 0.43, respectively. The ST sample has the highest Schmid factor. Therefore, it can be inferred that the ST sample has the lowest mechanical strength among the three specimens, while the SA sample is expected to have the highest mechanical strength, which is consistent with the results in Figure 6.

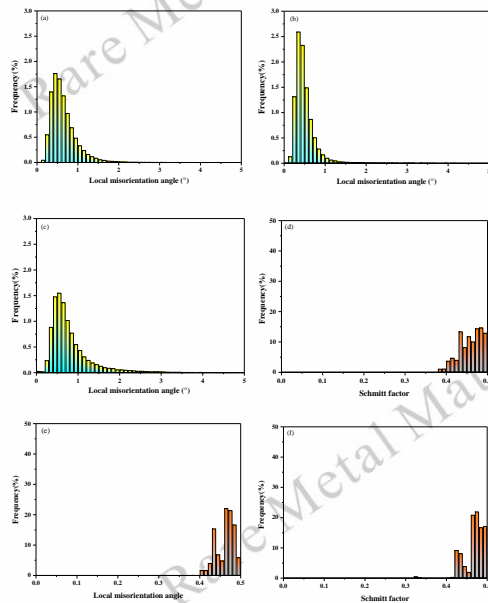


Fig. 14 Distribution of local misorientation angle of the grain boundaries of (a)AD; (b)ST; (c)SA. distribution of Schmidt factor for the three specimens (d)AD; (e)ST; (f)SA

### 3. Discussion

Carbide evolution plays an important role in the mechanical properties of nickel-based high temperature alloys<sup>[34,35]</sup>. Some topological close packed (TCP) phases and metal carbides (MC) are formed during prolonged high temperature exposure, which adversely affect the mechanical properties<sup>[36-38]</sup>. Carbides are the core of microporosity formation<sup>[39]</sup>, and for nickel-based high temperature alloys, crack sources in the alloys mainly sprout at carbides or eutectics<sup>[40]</sup>. The presence of nitrogen in the alloy leads to the generation of intracrystalline carbon-nitrides, which are more stable than carbides<sup>[14]</sup>, with enhanced intracrystalline strengthening. The eutectic

and carbon-nitride compounds of the AD sample are predominantly distributed between the dendrites. The size of the precipitates at the grain boundaries is larger than the size of the eutectic within the crystals (Fig. 9). As a result, cracks mainly sprout at grain boundaries, thus promoting the fracture of the alloy in the deformation process with a mixed fracture mechanism mainly along the grain. In addition, the element W added to the alloy is enriched in the precipitation phase and the matrix, and the element W is also a solid solution strengthening element, so W element can make the alloy have a stronger solid solution strengthening effect, which is one of the reasons leading to the nitrogenous nickel-based alloys with high yield strength. Precipitated phases on the grain boundaries of heat-treated samples are back dissolved or mostly remelted into the matrix (Fig. 10ab), and cracks can sprout at the edges of the intracrystalline precipitated phases, which leads to fracture of the alloy in high-temperature deformations by a hybrid fracture mechanism dominated by penetration of the crystals. Matrix-strengthened precipitates during aging process lead to a reduction in the elongation and cross-sectional shrinkage of the sample, and MC-type carbide particles can cause a deterioration of ductility at elevated temperatures<sup>[32]</sup>. The high YS of the SA sample can be attributed to the following factors: (i) Finer grain size and more uniform precipitation of strengthening phases. Figure 10b shows that the intragranular precipitates in the SA sample are smaller in size and have changed their shape from block-like in the as-deposited state to the current ellipsoidal shape, weakening the stress concentration. (ii) With most of the MC-type carbides on the grain boundaries re-dissolved into the matrix, it plays a solid solution strengthening effect. And  $M_{23}C_6$  on the grain boundaries plays a role in preventing the sliding of grain boundaries, so that the persistence of the alloy is improved<sup>[16, 17]</sup>. (iii) The presence of nitrogen in the alloy leads to a large amount of carbon-nitride generation within the grain, which is more stable than carbides<sup>[14]</sup>, and the strengthening effect of the intragranular strengthening is enhanced. (iv) A large number of strengthening phases  $\gamma'$  are present. As a result, the nitrogenous nickel-based alloys after aging have high yield strength, but at the same time low plasticity. The precipitates in the solid solution sample crystal are large in size and irregular in shape, and the angular precipitates can easily become the location of stress concentration (Fig. 10a), so mixed fracture mainly through the crystal will occur. At the same time, since there is no precipitated phase at the grain boundaries

that plays the role of pinning, the presence of precipitates can make the grain boundaries more zigzag and resist grain boundary sliding [41,42]. Therefore, the strength of solid solution sample is poor.

The microstructural investigation of AD and heat-treated specimens obtained by GMAW process allowed to propose a microstructure development model, which is summarized and graphically described in Fig. 15. It is particularly important to release segregated elements and reduce entangled vortex structures. Ageing treatment directly after solid solution promotes the formation of intergranular  $M_{23}C_6$  carbides and the strengthening phase  $\gamma'$  phase. It is also capable of inducing the precipitation of fine secondary carbide structures, which is particularly prominent in the strengthening effect. The consequences of these microstructural evolutions can be assessed by analyzing the tensile results and the associated fracture surface characteristics.

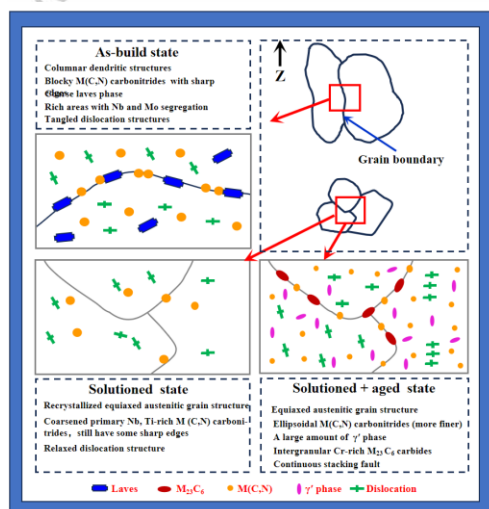


Fig. 15 Schematic of the major microstructure modifications occurring on nitrogenous nickel-based deposited metal samples fabricated by GMAW upon different heat treatment stages.

Through analysis using Oxford HKL Channel 5 software, it can be seen that the SA sample has a more uniform grain microstructure. Based on the local orientation deviations of the three samples, it can be inferred that the SA sample has the highest degree of deformation energy storage, while the ST sample has the lowest. By calculating the average Schmidt coefficient of three samples, it was found that the Schmid factor of the ST sample was the highest, while that of the SA sample was the lowest. In a specific slip system, the larger the Schmid factor, the easier it is to initiate the slip system when external stress is determined. Studies have shown that larger Schmid factors are more likely to cause grain deformation [30].

Therefore, it can be inferred that the ST sample has the lowest mechanical strength among the three samples, while the SA sample has the highest mechanical strength. These conclusions are also consistent with the results of the tensile test.

Plastic fracture damage is the result of a combination of local necking and microporous aggregation under various deformation conditions. After tensile fracture of the specimen, the alloy section as a whole becomes wedge-shaped, and some slip surfaces can also be observed. For polycrystalline nickel-based alloys, there are orientation deviations between different grains, so that different slip systems are initiated within different grains of the alloy during deformation for plastic deformation. Dislocations and laminations within different grains slip along the  $\{111\}$  surface and eventually accumulate near the grain boundaries, causing stress concentrations at the grain boundaries. With the accumulation of tensile deformation, the stress concentration at grain boundaries will gradually increase. When the stress concentrated at the grain boundary exceeds the strength of the grain boundary, it will lead to the formation of cracks along the grain. With the increase of temperature during heat treatment, the precipitated phase gradually dissolves back into the matrix, and the microscopic deformation mechanism changes from dislocation cutting of the precipitated phase system to dislocation sliding and climbing, and the stress concentration at the grain boundary can be relieved.

Entangled dislocations were observed in the microstructure of all three specimens after fracture. Since the transition group elements Co and W elements added to the composition of nitrogenous nickel-based flux-cored wires can significantly reduce the layer dislocation energy of the alloys [11,43], the nitrogenous nickel-based alloys have lower layer dislocation energies, which are favorable to the formation of layer dislocations. In the ST sample, some dislocation entanglement and a small amount of dislocation accumulation in the matrix channel can be observed. In the SA sample, some of entangled dislocations can be observed in the matrix, forming a substructure. Many laminar dislocations can also be seen, which also have a hindering effect on dislocation slip and provide a work-hardening effect. It has been suggested that laminar dislocations are formed by the decomposition of the matrix dislocation  $a/2\langle 101 \rangle$  into  $a/6\langle 121 \rangle$  Shockley incomplete dislocation and  $a/3\langle 112 \rangle$  leading dislocation at the interface of the matrix and the precipitated phase after  $a/3\langle 112 \rangle$  cuts into the

precipitated phase<sup>[44]</sup>. It has been proposed [45] that layer dislocations are formed by two Shockley incomplete dislocations together cutting into the precipitated phase. Regardless of the dislocation theory, it is a stacking fault left behind by an overtopping incomplete dislocation cutting into the precipitated phase. If the dislocations continue to slip, a continuous stacking fault is formed. The stacking faults in this article are also formed by this mechanism.

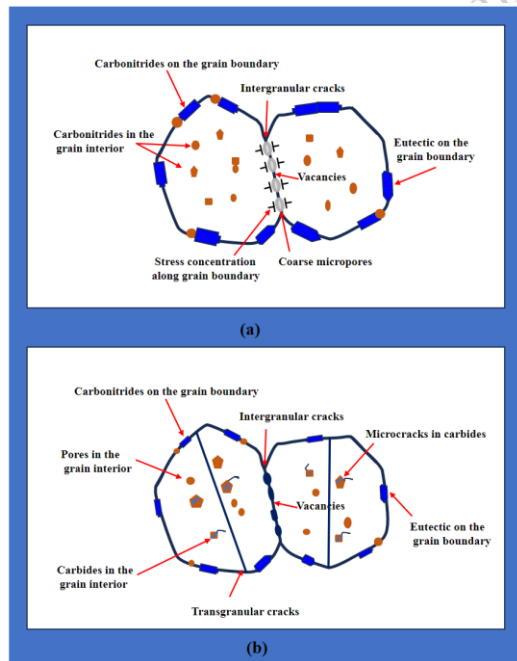


Fig. 16 Fracture behavior model (a) Fracture model in the medium to low temperature zone, (b) High temperature zone fracture model.

Research has shown that the fracture mode of nickel-based alloys at 600 °C is mainly mixed fracture with intergranular fracture<sup>[46]</sup>. This is due to the overall wedge shape of the cross-section of the alloy in this temperature interval, along with the presence of some sliding surfaces. For polycrystalline nickel-based alloys, there are orientation deviations between different grains. Alloys undergo plastic deformation by inducing different slip systems within different grains. Dislocations and stacking faults within different grains slide along the {111} plane and gather near grain boundaries, resulting in stress concentration at the grain boundaries. With the accumulation of tensile deformation, intergranular cracking occurs when the concentrated stress at the grain boundaries increases to a level that exceeds the strength of the grain boundaries. The crack source of nickel based high-temperature alloys usually comes from carbides or eutectic sites<sup>[15]</sup>. The size of carbides

at grain boundaries in this article is larger than the size of eutectics within the grains (Fig.10,11). Therefore, cracks mainly originate at grain boundaries, with intergranular fracture mechanism being the main mechanism. Figure 16 shows the model of intergranular crack propagation. In addition, stress and strain rate also have a certain influence. The strain rate in the tensile experiment of this article remains constant, while the rheological stress varies with temperature. When the rheological stress is at a high level, the coordination ability between grain boundaries cannot keep up with the deformation inside the grains. Sliding occurs between grain boundaries, resulting in intergranular cracks.

#### 4. Conclusions

This article uses the GMAW method to prepare nitrogenous nickel-based flux-cored welding wire deposited metal alloys, and studies the microstructure and mechanical properties of nitrogenous nickel-based flux-cored welding wire deposited metal in three different states. The results indicate that:

(1) The microstructure of nitrogenous nickel-based cladding metal is mainly composed of epitaxial growth of columnar grains. The alloy has large grains, with internal massive carbon-nitride generation. Due to the precipitation of Nb and Mo elements between the dendrites, a clustered Laves phase is formed between the dendrites in the final solidification stage. The Laves phase of the solid solution specimen is completely dissolved in the matrix and the carbides are partially dissolved. The SA sample formed  $M_{23}C_6$  carbides at grain boundaries as well as a small amount of elongated Laves phases, and nanoscale  $M(C,N)$  and a large amount of  $\gamma'$  phases precipitated within the grains.

(2) After solid solution and aging treatment, the alloy undergoes static recrystallisation, with coarse grains being replaced by equiaxed crystals. The heat-treated specimens have finer and more uniform grains with a stronger  $\langle 100 \rangle$  solidification texture. The average orientation deviations,  $K$ , of the nitrogenous nickel-based deposited metal in the as-deposited state as well as the ST state and the SA state were 0.94, 0.81 and 1.32, respectively.

(3) The yield strength and ultimate tensile stress of the nitrogenous nickel-based deposited metal in the as-deposited state were 416.51 MPa and 689.01 MPa, respectively, and the elongation was 26.81%. After the solid solution treatment, the yield strength and elongation were reduced, whereas the formation of a large number of  $\gamma'$  phases in the SA specimens as well as nanoscale  $M(C,N)$  precipitated in the crystal and

M<sub>23</sub>C<sub>6</sub> phases at the grain boundaries greatly increased the strength of the alloys, but reduced the elongation.

## References

- 1 A.H.V. Pavan, K.S.N. Vikrant, R. Ravibharath, Kulvir Singh. *Materials Science & Engineering A*[J],642 (2015) 32- 41.
- 2 C. Jang, J. Lee, J. Sung Kim, T. Eun Jin. *International Journal of Pressure Vessels and Piping*[J], 85 (2008) 635-646.
- 3 N. Pravin Kumar, N. Siva Shanmugam, G. Sreedhar. *Surface and Coatings Technology*[J], 415 (2021) 127138.
- 4 Guolonglong,Hualin Zheng,Liu Shaohu, et al.*Rare Metal Materials and Engineering*[J], 2016,45(9): 2219-2226.
- 5 P. Corigliano, V. Crupi. *Ocean Engineering*[J], 221 (2021), 108582.
- 6 S.L. Shang, D.E. Kim, C.L. Zacherl, Y. Wang, Y. Du, Z.K. Liu. *Journal of Applied Physics*[J], 112 (2012) 053515.
- 7 Y. Lin, C. Wang. *Computational Materials Science*[J], 195 (2021) 110447.
- 8 D. N. Duhl, C. P. Sullivan. *Journal of Metals*. [J], 1971, 23(7), 38-40.
- 9 R. Eriş, M.V. Akdeniz, A.O. Mekhrabov. *Metallurgical and Materials Transactions A*[J], 53 (2022) 1859-1872.
- 10 Zhao Ning, Tao Li, Guo Hui, Zhang Mengqi. *Rare Metal Materials and Engineering*[J], 2018,47(1):20-25.
- 11 A. Sengupta, S. K. Putatunda, L. Bartosiewicz, J. Hangas, P. J. Nailos, M. Peputapeck , F. E. Alberts. *Journal of Materials Engineering and Performance*[J], 1994, 3(1): 73-81.
- 12 Tongjai Chookajorn, Heather A. Murdoc, Christopher A. Schuh. *Science*[J],337 (2012) 951-954.
- 13 Kermanpur. A, Behjati. P, Han. J, et al. *Materials & Design*[J], 2015, 82(5): 273-280.
- 14 S. Fox, J.W. Brooks, M.H. Loretto, R.E. Smallman, *Strength of Metals and Alloys*, ICSMA J. 1 1985 399-401.
- 15 T. Liu, J.S. Dong, L. Wang, Z.J. Li, X.T. Zhou, L.H. Lou, J. Zhang. *Journal of Materials Science & Technology*[J], 31(2015) 269-279.
- 16 L. Z. HE, Q. ZHENG, X. F. SUN, G. C. HOU, H. R. GUAN, Z. Q. HU. *Journal of Materials Science*[J], 40 (2005) 2959-2964.
- 17 Huang Xuebing, Kang Yan, Zhou Huihua, Zhang Yun, Hu Zhuangqi. *Materials Letters*[J], 36 (1998) 210-213.
- 18 Qin. X. Z, Guo. J. T, Yuan. C, et al.. *Materials Science and Engineering A*[J], 2008, 485(1-2): 74-79.
- 19 Sajad Ghaemifar, Hamed Mirzadeh. *Journal of Materials Research and Technology* [J], 24 (2023) 3491-3501.
- 20 Qin. X. Z, Guo. J. T, Yuan. C, et al. *Metallurgical and Materials Transactions A*[J], 2007, 38(11): 3014-3022.
- 21 Abolfazl SAFARZADE, Mahmood SHARIFITABAR, Mahdi SHAFIEE AFARANI. *Transactions of Nonferrous Metals Society of China*[J],2020;30:3016-3030.
- 22 Mathieu Ternier, Jiwon Lee, et al. *Materials*[J], 2020;13(20):4643.
- 23 Huan Wang, Daijian Wu, Feng Xiao , Guozheng Quan, Bo Liu. *Materials Today Communications* [J], 2024.14.110673.
- 24 Mostafaei A, Behnamian Y, Krimer Y L, Stevens E L, Luo J L, Chmielus M. *Materials & Design* [J], 111 (2016):482-491.
- 25 ZHAOKUANG CHU, JINJIANG YU, et al. *Metallurgical and Materials Transactions A*[J], 2009; 40:2927-2937.
- 26 Giulio Marchese, et al., *Materials Science and Engineering: A*[J], 729 (2018) 64-75.
- 27 Yunlong Hu, Xin Lin, et al., *Materials Science and Engineering:A*[J], 817 (2021) 141309.
- 28 J.N. DuPont. *Metallurgical & Materials Transactions A*[J], 27 (1996) 3612-3620.
- 29 L.T. Khajavi, K. Morita, T. Yoshikawa, M. Barati, *Metallurgical and Materials Transactions B*[J], 46 (2015) 615-620.
- 30 T. Zhao, S. Zhang, et al., *Wear* [J], 510-511 (2022) 204510.
- 31 Yu Jinjiang, Lian Zhanwei, et al. *Materials Science and Engineering A* [J], 2010; 527:1896-1902.
- 32 G. Appa Rao a, Mahendra Kumar, M. Srinivas, D.S. Sarma. *Materials Science and Engineering A* [J], 355 (2003) 114-125.
- 33 G.P. Dinda, et al., *Scripta Materialia* [J], 67 (5) (2012) 503-506.
- 34 Heo. N. H, Chang. J. C, Kim. S. J. *Materials Science and Engineering A* [J], 2013, 559: 665-677.
- 35 Roy. A. K, Pal. J, Mukhopadhyay. C. *Materials Science and Engineering A* [J], 2008, 474(1-2): 363-370.
- 36 L. Tang, Q. Guo, C. Li, C. Liu, Y. Liu, *Journal of Materials Science & Technology*[J], 128 (2022) 180-194.

- 37 R. Krakow, D.N. Johnstone, A.S. Eggeman, D. Hünert, M.C. Hardy, C.M.F. Rae, P. A. Midgley. *Acta Materialia*[J], 130 (2017) 271-280.
- 38 K.R. Vishwakarma, N.L. Richards, M.C. Chaturvedi. *Materials Science & Engineering A*[J], 480 (2008) 517-528.
- 39 Y.C. Lin, Jiao Deng, Yu-Qiang Jiang, Dong-Xu Wen, Guan Liu. *Materials and Design*[J], 55 (2014) 949-957.
- 40 Beining Du, Jinxia Yang, Chuanyong Cui, Xiaofeng Sun. *Materials Science & Engineering A*[J], 623 (2015) 59-67.
- 41 Ramirez. A. J, Lippold. J. C. High temperature behavior of Ni-base weld metal –Part I. ductility and microstructural characterization[J]. *Materials Science and Engineering A*[J], 2004, 380: 259-271.
- 42 A. J Ramirez, J. C Lippold. *Materials Science and Engineering A*[J], 2004,380:245-258.
- 43 Nanseng. Y, Yuhuan. W, Hongzheng. F, Wengao. L, Rongde. T.. *Acta Metallurgica Sinica*[J], 1981, 17(1): 44-49.
- 44 Rae. C. M. F, Reed. R. C. *Acta Materialia* [J], 2007, 55(3): 1067-1081.
- 45 Viswanathan. G. B, Sarosi. P. M, Henry. M. F, et al. *Acta Materialia*[J], 2005, 53(10): 3041-3057.
- 46 Zhiyong Dai, Yunhai Su, Yingdi Wang, Taisen Yang, Xuewei Liang. *Materials Science and Engineering A*[J],2024, 903,146671.

## 新型含氮镍基熔敷金属从焊态到热处理的显微组织演变特征及力学性能

王英第<sup>1,2</sup>, 张桂清<sup>1</sup>, 杨太森<sup>1</sup>, 梁学伟<sup>1</sup>, 苏允海<sup>1\*</sup>

(1 沈阳工业大学 材料科学与工程学院, 沈阳 110870 )

(2 烟台职业学院 交通工程系, 烟台, 264670)

**摘要:** 本文采用 GMAW 焊制备了新型含氮镍基熔敷金属, 然后分别对其进行固溶处理、固溶和时效处理。研究了不同状态下的熔覆金属微观结构和拉伸性能的变化。结果表明, 添加 W 和 N 元素后, 沉积金属的高温抗拉强度表现良好。固溶处理后的样品晶粒尺寸减小, Laves 相消失, 但金属的屈服强度和伸长率都有所下降。固溶和时效处理后的样品晶粒尺寸更加均匀, 晶体析出了纳米级的 M(C, N) 相, 晶界处形成了 M<sub>23</sub>C<sub>6</sub> 相, 样品的屈服强度和极限拉伸强度均高于其他样品, 但塑性最低。主要变形机制是单位位错 a/2<110> 切削析出相。

**关键词:** 含氮沉积金属; 显微结构; 拉伸性能; 位错

**作者简介:** 王英第, 女, 1987 年生, 博士研究生, 沈阳工业大学 材料科学与工程学院, 辽宁 沈阳 110870, 电话: 18053556325, E-mail: wyy150403@163.com

**通讯作者:** 苏允海, 男, 1980 年生, 教授, 博士生导师, 沈阳工业大学 材料科学与工程学院, 辽宁 沈阳 110870, 电话: 13709840941, E-mail: su\_yunhai@sut.edu.cn